



Assembly of metals and nanoparticles into novel nanocomposite superstructures

Jiaquan Xu¹, Lianyi Chen^{1,2}, Hongseok Choi², Hiromi Konish³ & Xiaochun Li^{1,2}

¹Materials Science Program, University of Wisconsin-Madison, Madison, Wisconsin 53706, USA, ²Department of Mechanical Engineering, University of Wisconsin-Madison, Madison, Wisconsin 53706, USA, ³Department of Geoscience, University of Wisconsin-Madison, Madison, Wisconsin 53706, USA.

SUBJECT AREAS:
COMPOSITES
MOLECULAR SELF-ASSEMBLY
APPLIED PHYSICS
NANOPARTICLES

Received
25 January 2013

Accepted
9 April 2013

Published
25 April 2013

Correspondence and
requests for materials
should be addressed to
X.C.L. (xcli@engr.wisc.
edu)

Controlled assembly of nanoscale objects into superstructures is of tremendous interests. Many approaches have been developed to fabricate organic-nanoparticle superstructures. However, effective fabrication of inorganic-nanoparticle superstructures (such as nanoparticles linked by metals) remains a difficult challenge. Here we show a novel, general method to assemble metals and nanoparticles rationally into nanocomposite superstructures. Novel metal-nanoparticle superstructures are achieved by self-assembly of liquid metals and nanoparticles in immiscible liquids driven by reduction of free energy. Superstructures with various architectures, such as metal-core/nanoparticle-shell, nanocomposite-core/nanoparticle-shell, network of metal-linked core/shell nanostructures, and network of metal-linked nanoparticles, were successfully fabricated by simply tuning the volume ratio between nanoparticles and liquid metals. Our approach provides a simple, general way for fabrication of numerous metal-nanoparticle superstructures and enables a rational design of these novel superstructures with desired architectures for exciting applications.

Assembly of nano-scale objects into superstructures is an area of tremendous interests¹⁻⁷. After decades of intense investigations, many approaches have been developed to fabricate various superstructures. Most of them are organic-nanoparticle superstructures, nanoparticles connected by organic materials, e.g. organic molecules, polymers, DNA⁸⁻¹¹. The organic-nanoparticle superstructures exhibit unique properties and find broad applications. The parallel counterpart, inorganic-nanoparticle superstructures, nanoparticles connected by inorganic materials could also be significant for a wide range of applications, such as catalysts¹²⁻¹⁵, thermoelectric materials¹⁶, battery electrodes^{17,18}, magnetic materials^{12,19-22}, fuel cells¹⁵, solar cells^{13,23,24}, additives (for propellants, explosives, and pyrotechnic)^{25,26}, master nanocomposite²⁷, and structural components²⁸⁻³¹. At present, only limited inorganic nanocomposite superstructures were synthesized through wet colloidal chemical deposition of precursor components and sequential chemical reduction into desired components^{12,13,15,20,21,23,24,32}. The geometry of the superstructure highly depends on the organic media³³⁻³⁶. Expensive organometallics are widely used as the precursor^{13,23,24,32} for the creation of superstructures (e.g. nanoparticles linked by pure metal constituents). The chemical reduction process usually generates a large amount of effluents during the reaction process, demanding extensive post-processing^{37,38}. However, the self-assembly of most metals with nanoparticles into superstructures with controlled architectures remains an unresolved challenge, mainly due to the intrinsic properties of metals. Unlike aqueous or organic liquids, metals/alloys normally have high melting temperatures and greatly diminish the effect of electrostatic interactions, making nanoparticle dispersion and assembly in liquid metals an extremely difficult task.

Here we developed a novel methodology for self-assembly of metals (pure or alloyed) and nanoparticles into various metal-nanoparticle superstructures. The rapid assembly of liquid metals and nanoparticles is driven by the minimization of free energy in immiscible liquids, such as molten salts made of environmentally benign sodium chloride and potassium chloride. Superstructures of metal-core/nanoparticle-shell, nanocomposite-core/nanoparticle-shell, network of metal-linked core/shell nanostructures, and network of metal-linked nanoparticles were fabricated by simply tuning the volume ratio between nanoparticles and liquid metal. The approach reported here provides a versatile method of fabrication of numerous metal-nanoparticle superstructures and enables the rational design of metal-nanoparticle superstructures with desired architectures.

Results

Self-assembly of aluminum and TiCN nanoparticles into superstructures with various architectures in a molten salt made of eutectic of NaCl and KCl was used to demonstrate effectiveness of the novel approach. The stability of



the three phases is discussed in Supplementary Information. To assemble aluminum and TiCN nanoparticles into superstructures, the aluminum was heated above its melting point with TiCN nanoparticles in eutectic NaCl and KCl. Ultrasonic processing was used to disperse nanoparticles and molten aluminum in the molten salt uniformly. After ultrasonic processing, the liquid was cooled down to room temperature. Al-TiCN superstructures were obtained after solidification. The architecture of the superstructure obtained depends on the volume ratio between the nanoparticles to the Al, x . Detailed experimental procedure is described in Methods.

For the samples produced with a volume ratio, x , equal to 0.05, a representative scanning electron microscope (SEM) image (Figure 1a) suggests that the TiCN nanoparticles encapsulate the Al droplet. As further shown in Figure 1b, the scanning/transmission electron microscope (S/TEM) images of the cross section of the superstructures, revealed by focused ion beam (FIB), indicate that most nanoparticles stay on the surface of the Al spheres, forming metal-core/nanoparticle-shell superstructures.

For the samples produced with $x = 0.25$, a representative TEM image (Figure 1d) showed that TiCN nanoparticles fully cover the Al/molten salt interface. More interestingly, SEM images of the cross section, revealed by FIB, of the superstructures suggest that nanoparticles are well distributed inside the metal core, as shown in Figure 1e. This novel type of nano-structured superstructure morphology can be termed as nanocomposite-core/nanoparticle-shell

superstructure. The nanostructured superstructures produced with $x = 0.75$ and 1.0 (Figure 1f) possess a similar microstructure as that of the ones produced with $x = 0.25$, but with more nanoparticles staying inside the metal cores.

When x was further increased to 1.3, 1.5, and 2, nanoparticles were covered and bridged by Al films, forming a network of metal-linked core/shell nanostructures, as shown in Figure 2a. It is believed that nanoparticles and tiny Al droplets are initially dispersed inside the molten salt by the ultrasonic processing. The tiny Al droplets attach and spread on the surface of nanoparticles or nanoparticle clusters, forming a thin metal film (2–5 nm) (Figure 2b) on the nanoparticle surface. The Al liquid meniscus, or neck, between two nanoparticles causes an attractive capillary force^{39,40}, holding the nanoparticles together to form a three dimensional network.

When the volume ratio is further increased, the volume of Al is inadequate to fully cover the nanoparticle surfaces, leaving only the Al meniscus between nanoparticles to form a network of metal-linked nanoparticles, termed as pendular agglomeration. Figure 2d, Figure 2e, and Figure 2f display the representative microstructures of the samples with $x = 10$ and 20 (i.e. 4v% TiCN with 0.4v% and 0.2v% Al respectively in the molten salt). It clearly illustrates that nanoparticles are linked by nanoscale Al meniscus to form a porous network of metal-linked nanoparticles.

Discussion

Theoretical analysis was conducted to understand the experimental results. We define the interfacial energies of liquid Al/molten salt,

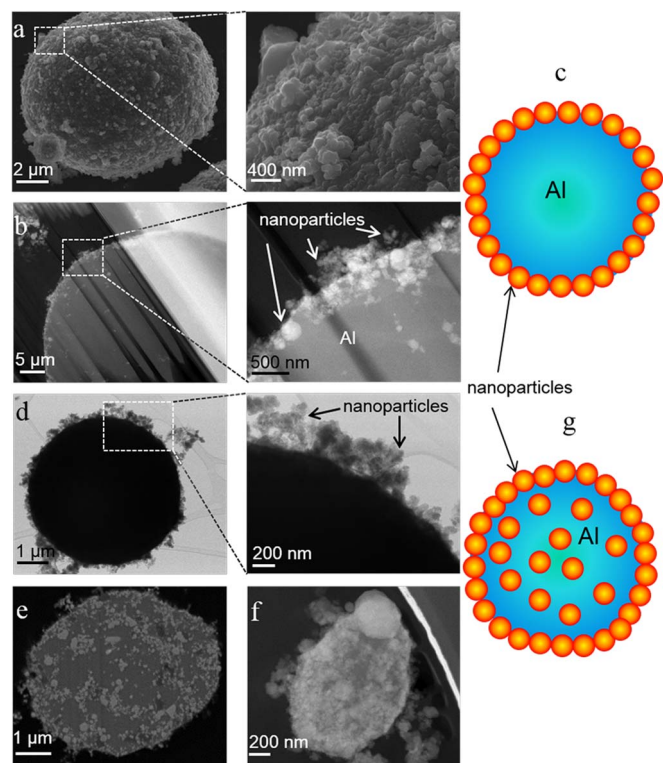


Figure 1 | Nanocomposite superstructures produced with $x < 1$: (a) Representative SEM images of samples with $x = 0.05$: the nanoparticles coated Al particle; (b) S/TEM images of the cross section of nanocomposite superstructures with $x = 0.05$. Most of the nanoparticles were on the surface and only a few inside the Al matrix; (c) Schematic of a Al-core/nanoparticle-shell superstructure; (d) TEM images of samples with $x = 0.25$: nanoparticles covered Al surface; (e) SEM image of the cross sections of samples with $x = 0.25$: nanoparticles covered Al sphere surface and distributed inside; (f) a S/TEM image of the cross-section of samples with $x = 1$: similar structure as $x=0.25$, but higher concentration of nanoparticles inside the matrix; (g) schematic of a nanocomposite-core/nanoparticle-shell superstructure.

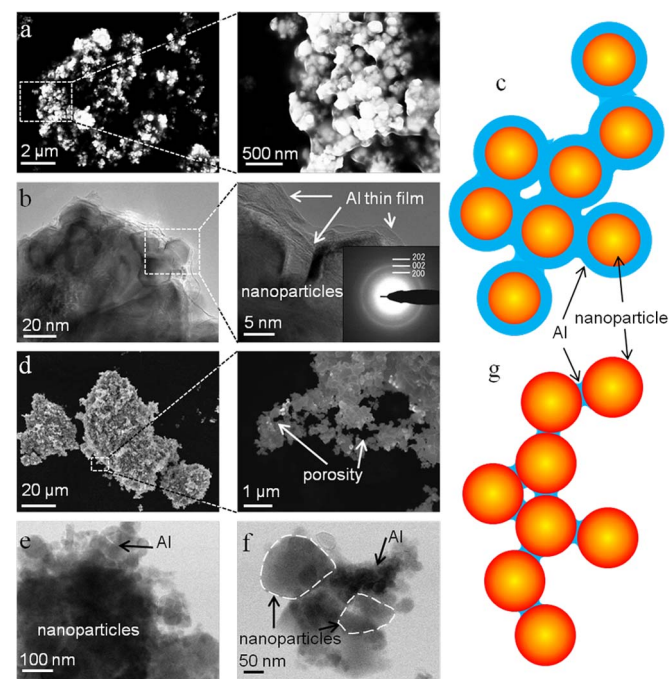


Figure 2 | Nanocomposites superstructures when $x > 1$: (a) SEM images of networks of a metal-linked core/shell nanostructure with $x = 1.5$; (b) TEM images of networks of a metal-linked core/shell nanostructure with $x = 1.5$, nanoparticles are covered and linked by Al thin film (Diffraction pattern of thin film was identified as AlOOH since Al thin film was exposed to the air. And AlOOH is parallel to (010) plane, only reflections from $h0l$ planes were recognized.); (c) schematic of networks of metal-linked core/shell nanostructures; (d) SEM images of networks of metal-linked nanoparticles with $x = 10$; (e) and (f) TEM images of the Al meniscus between nanoparticles for $x = 20$ sample (nanoparticle outline marked by dash line in f, EDX (Energy Dispersive X-Ray Analysis) of powders in f are in Figure S5 in the Supplementary Information); (g) schematic of networks of metal-linked nanoparticles.



molten salt/nanoparticle, and liquid Al/nanoparticles as σ_{AS} , σ_{SN} , σ_{AN} respectively. At equilibrium, Young's equation dictates the relationships between the interfacial energies and wetting angle, as defined shown in Figure 3a,

$$\sigma_{AN} + \sigma_{AS} \cos \theta = \sigma_{SN} \quad (1)$$

When the volume ratio is smaller than 1, the volume of Al droplets is larger than the volume of the nanoparticles. Thus, the configuration of the system is dictated by the interface between Al droplets and molten salt. Nanoparticles, as the third phase, could appear in the system in three possible states: nanoparticle inside the salt (defined as S1 as shown in Figure 3b), nanoparticle at the salt/Al interface (defined as S2 as shown in Figure 3c), and nanoparticle inside Al (defined as S3 as shown in Figure 3d). From open literatures, the value of σ_{AS} was estimated to be in a range from 0.72 to 0.78 N/m⁴¹ around the temperature of 700°C. However, for liquid aluminum and TiCN, there is no data or any direct methods for measuring σ_{AS} and σ_{SN} ⁴² from open literatures. Fortunately the data is not needed to conclude that S2 state is the most favorable state.

Since the wetting angle is not available, a quantitative analysis cannot be conducted. However, a reasonable qualitative analysis is still possible. TiCN, which consists of TiC and TiN, is a metallic ceramic, which will fundamentally tend to wet metals (metallic bond) more than the salt (ionic bond). Moreover, TiC and TiN wet Al melts well (wetting angle of TiC and TiN by Al melt is 0°⁴³ and 86°⁴⁴ respectively). It is reasonable to assume that TiCN would have a wetting angle of less than 90° with molten Al inside the salt⁴⁵.

Recalling the definition of Gibbs free energy, G :

$$G = E + pV - TS = U + \sigma A + pV - TS \quad (2)$$

Where E , P , V , T , S , U , σ , A are internal energy, pressure, volume, temperature, entropy, internal energy of all molecules in the bulk state, interfacial energy and interface area of the entire system, respectively. With a constant pressure, volume, temperature, and entropy and internal energy of all molecules in the bulk state, the Gibbs free energy of the three states are:

$$G_{S1} = U + pV - TS + 4\pi R^2 \sigma_{AS} + 4\pi r^2 \sigma_{SN} \quad (3)$$

$$G_{S2} = U + pV - TS + 4\pi R^2 \sigma_{AS} - \pi r^2 (1 + \cos^2 \theta) \sigma_{AS} + 2\pi r^2 \sigma_{AN} + 2\pi r^2 \sigma_{SN} \quad (4)$$

$$G_{S3} = U + pV - TS + 4\pi R^2 \sigma_{AS} + 4\pi r^2 \sigma_{AN} \quad (5)$$

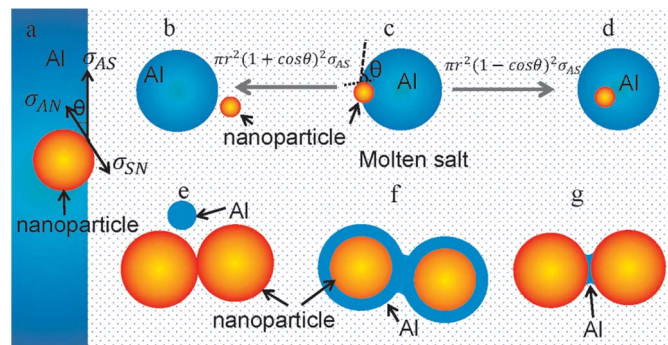


Figure 3 | Energy state analysis. (a) Schematic of wetting angle at equilibrium state; (b) a nanoparticle in molten salt phase (state S1); (c) a nanoparticle at the molten salt/Al interface (state S2); (d) a nanoparticle inside the Al phase (state S3); (e) Al forms a droplet in the molten salt phase (state S4); (f) Al spreads on the nanoparticle surfaces (state S5); (g) Al forms meniscus between nanoparticles (state S6). (Nanoparticles in a, e, f, g are enlarged to show details clearly).

When $\theta < 90^\circ$, which means that the Al liquid wets TiCN nanoparticles better than the molten salt, the free energy differences between the three states are⁴⁶

$$\begin{aligned} (G_{S1} - G_{S2}) &= \pi r^2 (1 + \cos \theta)^2 \sigma_{AS} > (G_{S3} - G_{S2}) \\ &= \pi r^2 (1 - \cos \theta)^2 \sigma_{AS} \geq 0 \end{aligned}$$

Thus S2 will be the most favorable state. It is expected that most nanoparticles would prefer to assemble at the molten salt/Al droplet interfaces. When the concentration of nanoparticles is low, almost all nanoparticles would assemble at the interface to reduce the free energy of the system, forming a nanoparticle coating on the Al droplets, which is schematically shown in Figure 1c and clearly validated by experimental results.

Moreover, as x increases, nanoparticles will envelop the interfacial area, and the S2 state would not be available for the additional nanoparticles. The nanoparticles are forced to migrate inside the Al droplets to secure the S3 state as a compromise, leading to form a metal matrix nanocomposite core inside the nanoparticle coating, as schematically shown in Figure 1g.

When $x > 1.0$, the volume of the nanoparticles is larger than that of the molten Al droplets in the immiscible molten salt liquid. Under this condition the surface coating and the interior volume of the Al droplets would not be able to contain all nanoparticles. Therefore, the interface between the nanoparticle and the molten salt take the primary role to determine the configuration of the system. Al droplets, as the third phase, could be positioned in this system with two possible states: Al droplets inside the molten salt (defined as S4 in Figure 3), and Al droplets at the nanoparticle/salt interface (defined as S5 in Figure 3). S4 is almost identical to the S1 state. The only difference is that the roles of Al droplets and nanoparticles are reversed. This is also the case with S5 and S2 states. Analogously, S5 is the energy favorable state. Molten Al droplets will tend to move onto the interface between the nanoparticles and the molten salt, then spread as Al thin films to cover the surfaces of the nanoparticles. The Al film will also naturally merge with neighbors, forming Al meniscus, to further minimize the free energy in the system, as shown in Figure 3f and Figure 3g. Depending on the content of the Al phase, Al meniscus with different sizes forms around the contact point between two nanoparticles, and the capillary forces resulting from the interfacial tension of the meniscus hold the nanoparticles together, forming networks of metal-linked core/shell nanostructures. The size and microstructure of the final networks are sensitive to the contents of nanoparticles and the Al phase. As x increases, the superstructure morphology will gradually change from networks of metal-linked core/shell nanostructures, to networks of metal-linked nanoparticles (S6 state in Figure 3g), shown in Figure 2c and Figure 2g.

The assembly of nanoparticles with liquid Al in molten salt was capable of producing metallic nanocomposite superstructures with four different morphologies. These could be of significance for broad technical applications. Al-core/nanoparticle-shell superstructures can be used to improve combustion properties and storage capability of Al powders, which are widely used as fuel additives to propellants, explosives, and pyrotechnic. In this work, molten salt were introduced to free the oxide film of Al powder and coat nanoparticles on the surfaces of Al powders, providing a scalable and low cost route for production of surface coated Al powders^{47,48}. Nanocomposite-core/nanoparticle-shell superstructures can be utilized as novel feedstock materials for sintering high performance metallic nanocomposites. They could also be utilized as master nanocomposites to be incorporated into various molten metals to fabricate diluted metallic nanocomposites. Three dimensional network superstructures, in the forms of capillary and pendular agglomeration of nanoparticles, have great potential in catalytic industries^{13,14}, electrode industries^{18,49,50} and possibly structural applications. Catalytic core/shell nanoparticles with rare metal elements as the shell were traditionally fabricated through laborious chemical approaches. The technology developed



in this study paves an efficient way for a scalable production of these novel nanostructured superstructures for widespread applications.

In summary, metal-nanoparticle superstructures with various architectures were fabricated by self-assembly of liquid metal and nanoparticles in molten salt made of environmentally benign eutectic sodium chloride and potassium chloride. The various architectures of the metal-nanoparticle superstructures, from metal-core/nanoparticle-shell, nanocomposite-core/nanoparticle-shell, networks of metal-linked core/shell nanostructures to networks of metal-linked nanoparticles, can be created by simply tuning the volume ratio between nanoparticles and liquid metal. The underlying mechanism of the self-assembly of these metal-nanoparticle superstructures is unraveled by the analysis of the Gibbs free energy. This work provides a general way for self-assembly of metal and nanoparticles into various superstructures, and enables a rational design of metal-nanoparticle superstructures with desired architectures.

Methods

Figure S2 in the Supplementary Information illustrates a schematic of the experimental setup, which consists of a resistance heating furnace, a gas protection system and an ultrasonic processing system. An alumina crucible with an outer diameter of 40 mm and a height of 95 mm was used for melting Al and the molten salt. In order to avoid oxidation of the liquid Al, the molten liquid was protected with argon gas at a constant flow rate through two gas nozzles. The ultrasonic processing system consists of an ultrasonic probe, a booster, and a transducer. A niobium ultrasonic probe with a diameter of 12.7 mm and a length of 92 mm was attached to the booster (Sonicator 3000, Misonix Inc.), which was mounted in the transducer working under a frequency of 20 kHz and a maximum 600 W power output.

TiCN nanoparticles (with an average diameter of 80 nm, from Sigma-Aldrich, see Appendix A) were mixed with 34.6 g KCl, 27.1 g NaCl and 3.6 g Al powder (with an average size of 44 μm , from Fisher Scientific, 99.0%) before the mixture was melted in the alumina crucible at 1000K under the protective argon gas. The tip of the niobium ultrasonic probe was inserted about 6 mm in depth into the melt. An ultrasonic vibration with a peak-to-peak amplitude of 60 μm was generated from the transducer. The melt was ultrasonically processed for 15 minutes to disperse nanoparticles and produce molten Al/molten salt emulsions. After the ultrasonic processing, the ultrasonic probe was lifted out of the melt. Then the crucible was taken out of the furnace to cool down in air. A spectrum of volume ratios, x , was tested, including 0, 0.05, 0.25, 0.75, 1.0, 1.2, 1.3, 1.5, 2, 10 and 20.

For microstructural characterizations, samples of about 10 g were cut from the solidified ingots. These small samples were then dissolved in 200 ml distilled water. The water solution of NaCl/KCl salt was then filtered through a filter paper with a mesh size of 0.7 μm to obtain powders. This process was repeated twice with another 200 ml water and 100 ml alcohol respectively. Finally the micro powders were dried in air. Field Emission Scanning Electron Microscopy (FESEM, LEO 1530, Carl Zeiss SMT), Focus Ion Beam (FIB, Carl Zeiss SMT), and Scanning/Transmission Electron Microscopy (S/TEM) were used for a detailed analysis of the surface coating and morphology for the powders. Specimen were prepared by mixing the powders with epoxy and sliced into thin pieces. FIB was also used to cut the powders open to reveal interior microstructures. The S/TEM analysis was conducted using a Titan-80-200 (FEI) microscope with an accelerating voltage of 200 kV. The size distribution of the powders was analyzed by use of a Mastersizer 2000E (Malvern Instruments Ltd).

- Min, Y. J., Akbulut, M., Kristiansen, K., Golan, Y. & Israelachvili, J. The role of interparticle and external forces in nanoparticle assembly. *Nat. Mater.* **7**, 527–538 (2008).
- Ryan, K. M., Mastroianni, A., Stancil, K. A., Liu, H. T. & Alivisatos, A. P. Electric-field-assisted assembly of perpendicularly oriented nanorod superlattices. *Nano Lett.* **6**, 1479–1482 (2006).
- Huang, Y., Duan, X. F., Wei, Q. Q. & Lieber, C. M. Directed assembly of one-dimensional nanostructures into functional networks. *Science* **291**, 630–633 (2001).
- Yang, P. D. Wires on water. *Nature* **425**, 243–244 (2003).
- Whitesides, G. M. & Grzybowski, B. Self-assembly at all scales. *Science* **295**, 2418–2421 (2002).
- Lin, Y., Skaff, H., Emrick, T., Dinsmore, A. D. & Russell, T. P. Nanoparticle assembly and transport at liquid-liquid interfaces. *Science* **299**, 226–229 (2003).
- Pochan, D. J. Approaching asymmetry and versatility in polymer assembly. *Science* **337**, 530–531 (2012).
- Rupar, P. A., Chabanne, L., Winnik, M. A. & Manners, I. Non-centrosymmetric cylindrical micelles by unidirectional growth. *Science* **337**, 559–562 (2012).
- Misza, K. *et al.* Hierarchical self-assembly of suspended branched colloidal nanocrystals into superlattice structures. *Nat. Mater.* **10**, 872–876 (2011).
- Boal, A. K. *et al.* Self-assembly of nanoparticles into structured spherical and network aggregates. *Nature* **404**, 746–748 (2000).
- Mirkin, C. A., Letsinger, R. L., Mucic, R. C. & Storhoff, J. J. A DNA-based method for rationally assembling nanoparticles into macroscopic materials. *Nature* **382**, 607–609 (1996).
- Nie, Z. H., Petukhova, A. & Kumacheva, E. Properties and emerging applications of self-assembled structures made from inorganic nanoparticles. *Nat. Nanotechnol.* **5**, 15–25 (2010).
- Subramanian, V., Wolf, E. E. & Kamat, P. V. Catalysis with TiO₂/gold nanocomposites. Effect of metal particle size on the Fermi level equilibration. *J. Am. Chem. Soc.* **126**, 4943–4950 (2004).
- Huber, D. L. Synthesis, properties, and applications of iron nanoparticles. *Small* **1**, 482–501 (2005).
- Alayoglu, S., Nilekar, A. U., Mavrikakis, M. & Eichhorn, B. Ru-Pt core-shell nanoparticles for preferential oxidation of carbon monoxide in hydrogen. *Nat. Mater.* **7**, 333–338 (2008).
- Liu, W., Yan, X., Chen, G. & Ren, Z. Recent advances in thermoelectric nanocomposites. *Nano Energy* **1**, 42–56 (2012).
- Vu, A., Qian, Y. & Stein, A. Porous electrode materials for lithium-ion batteries – how to prepare them and what makes them special. *Adv. Energy Mater.* **2**, 1056–1085 (2012).
- Zhang, B., Ye, D., Li, J., Zhu, X. & Liao, Q. Electrodeposition of Pd catalyst layer on graphite rod electrodes for direct formic acid oxidation. *J. Power Sources* **214**, 277–284 (2012).
- Vovchenko, L., Matzui, L., Stelmakh, O. & Zakharenko, A. Electric and magnetoresistance of nanocomposite material graphite-cobalt. *Fuller. Nanotub. Car. N.* **13**, 491–495 (2005).
- Cheon, J. *et al.* Magnetic superlattices and their nanoscale phase transition effects. *Proc. Nat. Acad. Sci. USA* **103**, 3023–3027 (2006).
- Cataldo, S., Pignataro, B., Ruggirello, A., Bongiorno, C. & Liveri, V. T. The zero field self-organization of cobalt/surfactant nanocomposite thin films. *Nanotechnology* **20**, 9 (2009).
- Walter, J. *et al.* Preparation of Rh-graphite and Rh-clay nanocomposites: Model substances for nanographite and induced magnetization in 4d transition metals. *J. Phys. Chem. B* **106**, 8547–8554 (2002).
- Hirakawa, T. & Kamat, P. V. Charge separation and catalytic activity of Ag@TiO₂ core-shell composite clusters under UV-irradiation. *J. Am. Chem. Soc.* **127**, 3928–3934 (2005).
- Wu, X. F., Song, H. Y., Yoon, J. M., Yu, Y. T. & Chen, Y. F. Synthesis of core-shell Au@TiO₂ nanoparticles with truncated wedge-shaped morphology and their photocatalytic properties. *Langmuir* **25**, 6438–6447 (2009).
- Chen, L., Song, W., Lv, J., Wang, L. & Xie, C. Effect of heating rates on TG-DTA analysis of aluminum nanopowders prepared by laser heating evaporation. *J. Therm. Anal. Calorim.* **96**, 141–145 (2009).
- Sun, Y. & Li, S. Combustion characteristics of coated nano aluminum in composite propellants. *Defense Sci. J.* **56**, 8 (2006).
- Wang, D., De Cicco, M. P. & Li, X. Using diluted master nanocomposites to achieve grain refinement and mechanical property enhancement in as-cast Al–9Mg. *Mater. Sci. Eng. A* **532**, 396–400 (2012).
- Cao, G., Konishi, H. & Li, X. Mechanical properties and microstructure of SiC-reinforced Mg-(2,4)Al-1Si nanocomposites fabricated by ultrasonic cavitation based solidification processing. *Mater. Sci. Eng. A* **486**, 357–362 (2008).
- De Cicco, M. *et al.* Strong, Ductile Magnesium-Zinc Nanocomposites. *Metall. Mater. Trans. A* **40A**, 3038–3045 (2009).
- Yang, Y. & Li, X. C. Ultrasonic cavitation-based nanomanufacturing of bulk aluminum matrix nanocomposites. *J. Manuf. Sci. E.-T. Asme* **129**, 252–255 (2007).
- Cao, G., Kobliska, J., Konishi, H. & Li, X. Tensile properties and microstructure of SiC nanoparticle-reinforced Mg-4Zn alloy fabricated by ultrasonic cavitation-based solidification processing. *Metall. Mater. Trans. A* **39A**, 880–886 (2008).
- de Oca, M. G. M., Plana, D., Ceorrio, V., Lazaro, M. J. & Fermin, D. J. Electrochemical properties of strained Pd nanoshells at Au nanostructures: CO and HCOOH oxidation. *J. Phys. Chem. C* **116**, 692–699 (2012).
- Patil, A. J. & Mann, S. Self-assembly of bio-inorganic nanohybrids using organoclay building blocks. *J. Mater. Chem.* **18**, 4605–4615 (2008).
- Lin, Y. L. *et al.* Self-assembled superstructures of polymer-grafted nanoparticles: effects of particle shape and matrix polymer. *J. Phys. Chem. C* **115**, 5566–5577 (2011).
- Akcora, P. *et al.* Anisotropic self-assembly of spherical polymer-grafted nanoparticles. *Nat. Mater.* **8**, 354–359 (2009).
- Yan, L. T., Popp, N., Ghosh, S. K. & Boker, A. Self-assembly of Janus nanoparticles in diblock copolymers. *ACS Nano* **4**, 913–920 (2010).
- Belman, N. *et al.* Hierarchical superstructure of alkylamine-coated ZnS nanoparticle assemblies. *Phys. Chem. Chem. Phys.* **13**, 4974–4979 (2011).
- Gao, Y. & Tang, Z. Y. Design and application of inorganic nanoparticle superstructures: current status and future challenges. *Small* **7**, 2133–2146 (2011).
- Koos, E. & Willenbacher, N. Capillary forces in suspension rheology. *Science* **331**, 897–900 (2011).
- Butt, H. J. & Kappl, M. Normal capillary forces. *Adv. Colloid Interface Sci.* **146**, 48–60 (2009).
- Lopez, V. H. & Kennedy, A. R. Flux-assisted wetting and spreading of Al on TiC. *J. Colloid Interface Sci.* **298**, 356–362 (2006).
- Binks, B. P. & Clint, J. H. Solid wettability from surface energy components: Relevance to pickering emulsions. *Langmuir* **18**, 1270–1273 (2002).



43. Liu, L. M., Wang, S. Q. & Ye, H. Q. Adhesion and bonding of the Al/TiC interface. *Surf. Sci.* **550**, 46–56 (2004).
44. Kaptay, G., Bader, E. & Bolyan, L. Interfacial forces and energies relevant to production of metal matrix composites. *Mater. Sci. Forum* **329–3**, 151–156 (2000).
45. De Dicco, M. P., Dake, W. & Xiaochun, L. An investigation of nanoparticle wetting, grain refinement, and mechanical property enhancement in Al matrix nanocomposites. *TMS (The Minerals, Metals & Materials Society)* **123** (2011).
46. Aveyard, R., Binks, B. P. & Clint, J. H. Emulsions stabilised solely by colloidal particles. *Adv. Colloid Interface Sci.* **100**, 503–546 (2003).
47. Kwon, Y. S. *et al.* Features of passivation, oxidation and combustion of tungsten nanopowders by air. *Int. J. Refract. Met. H.* **22**, 235–241 (2004).
48. Yagodnikov, D. A., Andreev, E. A., Vorob'ev, V. S. & Glotov, O. G. Ignition, combustion, and agglomeration of encapsulated aluminum particles in a composite solid propellant. I. Theoretical study of the ignition and combustion of aluminum with fluorine-containing coatings. *Combustion Explosion and Shock Waves* **42**, 534–542 (2006).
49. Cui, L. F., Hu, L. B., Choi, J. W. & Cui, Y. Light-weight free-standing carbon nanotube-silicon films for anodes of lithium ion batteries. *ACS Nano* **4**, 3671–3678 (2010).
50. Shao, Y. Y., Liu, J., Wang, Y. & Lin, Y. H. Novel catalyst support materials for PEM fuel cells: current status and future prospects. *J. Mater. Chem.* **19**, 46–59 (2009).

Acknowledgments

This work is supported by National Institute of Standards and Technology (NIST) through its Technology Innovation Program.

Author contributions

J.Q. X. conducted the experiments and thermodynamic analysis. L.Y. C. conducted the experiments and data analysis. H.S. C. conducted the initial experiments to prove the concept. H. K. performed TEM study. X.C. L. conceived the idea and supervised the work. J.Q. X., L.Y. C. and X.C. L. wrote the paper.

Additional information

Supplementary information accompanies this paper at <http://www.nature.com/scientificreports>

Competing financial interests: The authors declare no competing financial interests.

License: This work is licensed under a Creative Commons Attribution-NonCommercial-NoDerivs 3.0 Unported License. To view a copy of this license, visit <http://creativecommons.org/licenses/by-nc-nd/3.0/>

How to cite this article: Xu, J.Q., Chen, L.Y., Choi, H., Konish, H. & Li, X.C. Assembly of metals and nanoparticles into novel nanocomposite superstructures. *Sci. Rep.* **3**, 1730; DOI:10.1038/srep01730 (2013).